



Submitted to

Charged current interactions in ep scattering at HERA with longitudinally polarised lepton beams

H1 Collaboration

Abstract

Data taken with e^\pm beams of different longitudinal polarisation states in collision with unpolarised protons at HERA are used to measure the total cross sections of the charged current process, $e^\pm p \rightarrow \nu X$, for negative four-momentum transfer squared $Q^2 > 400 \text{ GeV}^2$ and inelasticity $y < 0.9$. Together with the corresponding cross section obtained from the previously published unpolarised data, the polarisation dependence of the charged current cross section is measured and found to be in agreement with the Standard Model prediction. The data are also used to measure the single and double differential reduced cross sections $d\sigma/dQ^2$ and $\tilde{\sigma}(x, Q^2)$ using the complete HERA-II data set.

1 Introduction

Measurements of deep inelastic scattering (DIS) with polarised leptons on protons allow the parton distribution functions (PDFs) of the proton to be further constrained through polarisation asymmetries [1] and specific tests of the electroweak (EW) parts of the Standard Model to be performed [2, 3]. In particular, the measurements presented here extend the tests of the $V - A$ structure of charged current interactions from low Q^2 [4] into the high Q^2 regime, where Q^2 is the negative four-momentum transfer squared.

At HERA DIS proceeding via charged currents (CC), $ep \rightarrow \nu X$, and neutral currents (NC), $ep \rightarrow eX$, can be measured accurately [5, 6, 7, 8]. The polarisation dependence of the CC and NC cross sections is fixed within the Standard Model framework. Specifically, the Standard Model predicts, from the absence of right handed charged currents, that the CC e^-p cross section is directly proportional to the fraction of left handed electrons in the beam.

In this paper measurements of the charged current cross sections, $\sigma_{\text{CC}}^{\text{tot}}$, $d\sigma/dQ^2$ and the reduced double differential cross section $\tilde{\sigma}(x, Q^2)$ are reported for two values of longitudinal polarisation, $P_e = (N_R - N_L)/(N_R + N_L)$, with N_R (N_L) being the number of right (left) handed leptons in the beam. The corresponding data sets are termed the R and L data sets respectively. The corresponding luminosity and longitudinal lepton beam polarisation is given in Tab. 1 below.

	R	L
e^-p	$\mathcal{L} = 45.9 \text{ pb}^{-1}$ $P_e = (+36.9 \pm 2.3)\%$	$\mathcal{L} = 103.2 \text{ pb}^{-1}$ $P_e = (-26.1 \pm 1.0)\%$
e^+p	$\mathcal{L} = 98.1 \text{ pb}^{-1}$ $P_e = (+32.5 \pm 1.2)\%$	$\mathcal{L} = 81.9 \text{ pb}^{-1}$ $P_e = (-37.6 \pm 1.4)\%$

Table 1: Table of integrated luminosities, \mathcal{L} , and luminosity weighted longitudinal polarisation, P_e for the data sets presented here.

2 Charged Current Cross Section

The measured double differential CC cross section for collisions of polarised electrons with unpolarised protons, corrected for QED radiative effects, may be expressed as

$$\frac{d^2\sigma_{\text{CC}}^{\pm}}{dx dQ^2} = (1 - P_e) \frac{G_F^2}{4\pi x} \left[\frac{M_W^2}{M_W^2 + Q^2} \right]^2 (Y_+ W_2^{\pm} - Y_{\mp} x W_3^{\pm} - y^2 W_L^{\pm}) \cdot (1 + \delta_{\text{weak}}^{\text{CC}}), \quad (1)$$

where x is the Bjorken x variable and y characterises the inelasticity of the interaction. The Fermi constant G_F is defined [9] using the weak boson masses. Other quantities in Eq.(1) include M_W , the mass of the W boson, W_2^{\pm} , xW_3^{\pm} and W_L^{\pm} , CC structure functions for $e^{\pm}p$ scattering, and $\delta_{\text{weak}}^{\text{CC}}$, the weak radiative corrections. The helicity dependences of the weak interaction are contained in $Y_{\pm} = 1 \pm (1 - y)^2$. In the quark parton model (QPM), where

$W_L^\pm \equiv 0$, the structure functions W_2^\pm and xW_3^\pm may be expressed as the sum and difference of the quark and anti-quark momentum distributions, $xq(x, Q^2)$ and $x\bar{q}(x, Q^2)$:

$$W_2^- = x(u + c + \bar{d} + \bar{s}), W_2^+ = x(\bar{u} + \bar{c} + d + s), \quad (2)$$

$$xW_3^- = x(u + c - \bar{d} - \bar{s}), xW_3^+ = x(d + s - \bar{u} - \bar{c}) \quad (3)$$

The total cross section, σ_{CC}^{tot} , is defined as the integrated cross section in the kinematic region $Q^2 > 400 \text{ GeV}^2$ and $y < 0.9$. From Eq.(1) it can be seen that the cross section has a linear dependence on the polarisation of the electron beam P_e . For a fully right handed electron beam, $P_e = 1$, or a fully left handed positron beam the cross section is identically zero in the Standard Model.

3 Experimental Technique

At HERA transverse polarisation of the lepton beam arises naturally through synchrotron radiation via the Sokolov-Ternov effect [10]. In 2000 a pair of spin rotators was installed in the beamline on either side of the H1 detector, allowing transversely polarised leptons to be rotated into longitudinally polarised states and back again. The degree of polarisation is constant around the HERA ring and is continuously measured using two independent polarimeters LPOL [11] and TPOL [12]. The polarimeters are situated in beamline sections in which the beam leptons have longitudinal and transverse polarisations respectively. Both measurements rely on an asymmetry in the energy spectrum of left and right handed circularly polarised photons undergoing Compton scattering with the lepton beam. The TPOL measurement uses in addition a spatial asymmetry. The LPOL polarimeter measurements are used when available and TPOL measurements otherwise. The polarisation profile weighted by the luminosity values is shown in Fig. 1.

The H1 detector components most relevant to this analysis are the liquid argon (LAr) calorimeter, which measures the positions and energies of charged and neutral particles over the polar¹ angular range $4^\circ < \theta < 154^\circ$, and the inner tracking detectors, which measure the angles and momenta of charged particles over the range $7^\circ < \theta < 165^\circ$. A full description of the detector can be found in [13].

Simulated DIS events are used in order to determine acceptance corrections. DIS processes are generated using the DJANGO [14] Monte Carlo (MC) simulation program, which is based on LEPTO [15] for the hard interaction and HERACLES [16] for single photon emission and virtual EW corrections. LEPTO combines $\mathcal{O}(\alpha_s)$ matrix elements with higher order QCD effects using the colour dipole model as implemented in ARIADNE [17]. The JETSET program [18] is used to simulate the hadronisation process. In the event generation the DIS cross section is calculated using the H1 PDF 2009 [8] parametrisation for the proton PDFs.

The dominant ep background contribution arises from photoproduction processes. These are simulated using the PYTHIA [19] MC with leading order PDFs for the proton taken from CTEQ [20] and for the photon from GRV [21]. Further backgrounds from NC DIS, QED-Compton scattering, lepton pair production, prompt photon production and heavy gauge boson

¹The polar angle θ is defined with respect to the positive z axis, the direction of the incident proton beam.

(W^\pm, Z^0) production are also simulated; their final contribution to the analysis sample is small. Further details are given in [6].

The detector response to events produced by the generation programs is simulated in detail using a program based on GEANT [22]. These simulated events are then subjected to the same reconstruction and analysis chain as the data.

The selection of CC interactions follows closely that of the previously published analysis of unpolarised data from H1 [6] and is briefly described below. The CC events are characterised as having large unbalanced transverse momentum, $P_{T,h}$, attributed to the undetected neutrino. The quantity $P_{T,h}$ is determined from $P_{T,h} = \sqrt{(\sum_i p_{x,i})^2 + (\sum_i p_{y,i})^2}$, where the summation is performed over all particles of the hadronic final state. The hadronic final state particles are reconstructed using a combination of tracks and calorimeter deposits in an energy flow algorithm that avoids double counting [23].

The CC kinematic quantities are determined from the hadronic final state [24] using the relations

$$y_h = \frac{E_h - p_{z,h}}{2 E_e}, \quad Q_h^2 = \frac{P_{T,h}^2}{1 - y_h}, \quad x_h = \frac{Q_h^2}{s y_h}, \quad (4)$$

where $E_h - p_{z,h} \equiv \sum_i (E_i - p_{z,i})$ and E_e is the incident electron beam energy.

NC interactions are also studied as they provide an accurate and high statistics data sample with which to check the detector response. The selection of NC interactions is based mainly on the requirement of an identified scattered electron in the LAr calorimeter, with an energy $E'_e > 11$ GeV. The NC sample is used to carry out an *in-situ* calibration of the electromagnetic and hadronic energy scales of the LAr calorimeter using the method described in [6, 23, 25, 26]. The hadronic calibration procedure is based on the balance of the transverse energy of the electrons with that of the hadronic final state. The calibration procedure gives good agreement between data and simulation within an estimated uncertainty of 2% on the hadronic scale.

In addition, NC events are used for studies of systematic uncertainties in the charged current analysis. The data are processed such that all information from the scattered electron is suppressed, providing the so-called *pseudo-CC* sample [23, 25, 26, 27]. This sample mimics CC interactions allowing trigger and selection efficiencies to be checked with high statistical precision and independently of the MC simulation.

4 Measurement Procedure

Candidate CC interactions are selected by requiring $P_{T,h} > 12$ GeV and a reconstructed vertex within 35 cm in z of the nominal interaction point. In order to ensure high efficiency of the trigger and good kinematic resolution the analysis is further restricted to the domain of $0.03 < y_h < 0.85$. The ep background is dominantly due to photoproduction events, in which the scattered electron escapes undetected in the backward direction and transverse momentum is missing due to fluctuations in the detector response or undetected particles. This background is suppressed exploiting the correlation between $P_{T,h}$ and the ratio V_{ap}/V_p of transverse energy flow anti-parallel and parallel to the hadronic final state transverse momentum vector [23, 25,

26]. The suppression cuts are different for the R and L data sets as the relative photoproduction contributions differ in the two samples. The residual ep background is negligible for most of the measured kinematic domain. The simulation is used to estimate this contribution, which is subtracted statistically from the CC data sample. Non- ep background is rejected by searching for typical cosmic ray and beam-induced background event topologies [23, 25, 26].

The Q_h^2 , $P_{T,h}$, $E_h - p_{z,h}$ and x_h distributions of the selected events are shown in Figs. ?? and 3 for the L (upper) and R (lower) samples. The simulation provides a good description of the data. The contribution of background photoproduction processes is small and has the largest influence at low $P_{T,h}$.

Events with $Q_h^2 > 400 \text{ GeV}^2$ are used to measure the cross sections, which correspond to the kinematic region $Q^2 > 400 \text{ GeV}^2$ and $y < 0.9$ and thus are corrected for the effects of the analysis cuts. The correction factor is calculated to be 1.07 using the H1 PDF 2009 parametrisation.

The systematic uncertainties on the cross section measurements are discussed briefly below (see [23, 25, 26] and references therein for more details). Positive and negative variations of one standard deviation of each error source are found to yield errors which are symmetric to a good approximation. The systematic uncertainties of each source are taken to be fully correlated between the cross section measurements unless stated otherwise.

- An uncertainty of 2% is assigned to the scale of the hadronic energy measured in the LAr calorimeter, of which 1% is considered as a correlated component to the uncertainty. This results in a total uncertainty of 1.3% on the cross section measurements.
- A 10% uncertainty is assigned to the amount of energy in the LAr calorimeter attributed to noise, which gives rise to a systematic error of 0.3% on the cross section measurements.
- The variation of cuts against photoproduction on V_{ap}/V_p and $P_{T,h}$ has an effect on the cross sections of 0.6%.
- A 30% uncertainty on the subtracted ep background is determined from a comparison of data and simulation after relaxing the anti-photoproduction cuts, such that the sample is dominated by photoproduction events.
- The non- ep background finders introduce an inefficiency for CC events. The associated uncertainty is estimated using pseudo-CC data and found to depend on y . The uncertainty is 2% for $y < 0.1$ and 1% for $y > 0.1$.
- A y -dependent error is assigned to the vertex finding efficiency: An uncertainty of 1% is applied for $y > 0.15$, 4% for $0.15 > y > 0.06$, and 15% for $y < 0.06$. This yields an uncertainty of $\simeq 2\%$ on the total cross section measurements.
- An uncertainty of 0.5% accounts for the dependence of the acceptance correction on the PDFs used in the MC simulation.
- A 1.8% uncertainty on the trigger efficiency is determined based on the pseudo-CC data sample. The uncorrelated component of this uncertainty is 1%.

- An error of 0.8% is estimated for the QED radiative corrections. This accounts for missing contributions in the simulation of the lowest order QED effects and for the uncertainty on the higher order QED and EW corrections.
- In addition, there is a global uncertainty of 2.1% on the luminosity measurement for both the R and L data samples, of which 0.5% is considered as correlated.
- The relative uncertainty in the measurement of the lepton beam polarisation is taken to be 1.6% for the LPOL and 3.5% for the TPOL [28], yielding a total relative polarisation uncertainty in the e^+p sample of 1.2% for the R data set and 1.4% for the L data set. For the e^-p data a relative uncertainty of 2.3% for the R data set and 1.0% for the L data set is obtained. These uncertainties are not included in the error bars of the data points.

The total systematic error is formed by adding the individual uncertainties in quadrature and amounts to about 4% on the total cross section measurements.

5 Results

The measured integrated CC cross sections are quoted in the range $Q^2 > 400 \text{ GeV}^2$ and $y < 0.9$ and are given in Tab. 2 and shown in Figs. 4 and 5. The measurement of the unpolarised total cross section in the same phase space based on HERA-I data is also given. This measurement follows identically the procedure described in [29] but with the Q^2 cut adopted in this analysis. The systematic uncertainties of this unpolarised measurement are taken to be the same as in [6], with the exception of the QED radiative correction uncertainty, which has been reduced from 3% to 0.8%. The measurements are compared to expectations of the Standard Model using the H1 PDF 2009 parametrisation. The uncertainty on the Standard Model expectations combines the uncertainties from experimental data used in the H1 PDF 2009 fit as well as model uncertainties [8].

The data exhibit a clear linear polarisation dependence of the cross sections which is maximal for left handed e^-p scattering and right handed e^+p scattering demonstrating the parity violation of purely weak charged current interactions.

	P_e (%)	$\sigma_{\text{CC}}^{\text{tot}}$ (pb)	SM expectation (pb)
e^-p	+36.9	$36.3 \pm 1.1_{\text{stat}} \pm 1.0_{\text{sys}}$	$37.3^{+1.0}_{-0.8}$
	0.0	$57.0 \pm 2.2_{\text{stat}} \pm 1.4_{\text{sys}}$	$59.2^{+1.6}_{-1.3}$
	-26.1	$71.0 \pm 1.1_{\text{stat}} \pm 2.0_{\text{sys}}$	$74.5^{+2.0}_{-1.6}$
e^+p	+32.5	$39.2 \pm 0.8_{\text{stat}} \pm 1.4_{\text{sys}}$	$37.8^{+1.1}_{-0.8}$
	0.0	$28.4 \pm 0.8_{\text{stat}} \pm 0.8_{\text{sys}}$	$28.5^{+0.9}_{-0.3}$
	-37.6	$17.8 \pm 0.6_{\text{stat}} \pm 0.6_{\text{sys}}$	$17.8^{+0.5}_{-0.3}$

Table 2: Measured cross section values for $\sigma_{\text{CC}}^{\text{tot}}$ in the region $Q^2 > 400 \text{ GeV}^2$ and $y < 0.9$ compared to the Standard Model (SM) expectation from H1 PDF 2009.

Measurements of the single differential cross sections $d\sigma/dQ^2$ have also been made for the L and R samples in $e^\pm p$ scattering. These are shown in Figs. 6 and 7 compared to the Standard Model expectation based on the PDFs from H1 PDF 2009. The cross sections are observed to fall with increasing Q^2 and have a more rapid decrease for $Q^2 > 2000 \text{ GeV}^2$. In the context of the Standard Model this is understood to arise from the falling parton densities as Q^2 (and hence also x) increases. Close to the Electroweak scale the influence of the heavy W^\pm propagator ($\sim [M_W^2/(Q^2 + M_W^2)]^2$) causes a further suppression of the cross section.

The performance of the Standard Model in being able to describe these cross section measurements is better seen in Figs. 8 and 9 where the ratio of the measured cross sections to the Standard Model expectations using the H1 PDF 2009 partons is shown. Also visible is the ratio using the HERAPDF1.0 partons. The Standard Model provides a good description of the measured cross sections in both shape and normalisation, although it is noted that the e^-p L data lie systematically below the prediction by about 2 – 3% (where the normalisation uncertainty is $\pm 2.1\%$). The data are in better agreement with the HERAPDF1.0 expectation.

The charged current cross section is largest for e^-p left polarised scattering ($P_e < 0$) and with the given integrated luminosity these measured cross sections have a precision which is approximately balanced between the statistical and systematic uncertainties. In all other samples the data are limited by their statistical uncertainty. This uncertainty can be reduced by combining the L and R samples into an effective unpolarised data set (correcting for the small residual polarisation). The resulting cross sections are then combined with previously published H1 measurements of the unpolarised cross sections [31, 29, 6]. The method of combination is described in detail in [7]. This method forms a model independent average from several measurements of the same cross section taking into account the systematic uncertainties correlated across the data sets. The final combined cross sections make use of the complete HERA dataset collected by H1 and amounts to a total luminosity of 165.5 pb^{-1} for e^-p scattering and 280.8 pb^{-1} for e^+p scattering. The combined cross sections are shown in Figs. 10 and 11 where again it can be seen that the expectation from H1 PDF 2009 provides an excellent description of the data. The cross section ratios to the Standard Model expectation using the H1 PDF 2009 partons are shown in Fig. 12.

In order to obtain the best sensitivity to the PDFs the double differential reduced cross sections σ_{CC}^{tot} are measured for each of the four data sets, $e^\pm p$ for the R and L polarised samples. The cross sections are shown in Figs. 13 and 14 for electron scattering and positron scattering respectively.

These data are combined into an effective unpolarised measurement after correcting for the residual polarisation, and then further combined with unpolarised measurements from HERA-I as described earlier. These measurements using the complete HERA-I+II data sets are shown in Figs. 15 and 16 for electron and positron scattering respectively. The expectation to the Standard Model using H1 PDF 2009 is shown as the shaded band.

The leading order quark and anti-quark contributions to the reduced cross sections are shown for the electron and positron scattering data in Figs. 17 and 18 respectively. In the former case the cross section is everywhere dominated by the up-type quark contributions from u and c . This is due to the small sea quark contribution at high x and the $(1 - y)^2$ helicity suppression of anti-quarks at low x . However, in the case of positron scattering this helicity suppression

factor affects the down-type quarks at low x . At high x the large d valence distribution is unsuppressed, thus CC measurements in e^+p can provide stringent constraints on the high x d valence PDF.

In Fig. 19 the Q^2 dependence of the cross section measurements from H1 and ZEUS are shown for unpolarised charged lepton scattering in both the neutral and charged current channels. The HERAPDF 1.0 fit is compared to the data and shows good agreement across the range of the measurements.

6 Summary

Measurements of polarised $e^\pm p$ charged current cross sections σ_{CC}^{tot} , $d\sigma/dQ^2$ and $\tilde{\sigma}(x, Q^2)$ using the complete HERA-II data set have been reported. The results are based on data collected from collisions of unpolarised protons with polarised electron and positron beams in left and right helicity states. The polarisation dependence of the charged current cross section has thus been established at HERA both in e^+p and in e^-p collisions, extending previous tests of the chiral structure of the charged current interaction into the region of large, space-like Q^2 . The data are found to be consistent with the Standard Model axiomatic absence of right handed charged currents.

The statistical uncertainty of the differential measurements is reduced by combining the HERA-I and HERA-II data to yield unpolarised differential cross sections with a total luminosity of 165.5 pb^{-1} for e^-p scattering and 280.8 pb^{-1} for e^+p scattering.

Acknowledgements

We are grateful to the HERA machine group whose outstanding efforts have made this experiment possible. We thank the engineers and technicians for their work in constructing and maintaining the H1 detector, our funding agencies for financial support, the DESY technical staff for continual assistance and the DESY directorate for support and for the hospitality which they extend to the non DESY members of the collaboration.

References

- [1] M. Klein and T. Riemann, *Z. Phys. C* **24** (1984) 151.
- [2] A. Aktas *et al.* [H1 Collaboration], *Phys. Lett. B* **632** (2006) 35 [hep-ex/0507080].
- [3] R. Beyer *et al.*, Proceedings of the Workshop “Future Physics at HERA”, vol. 1, eds. W. Buchmüller, G. Ingelman, A. De Roeck and R. Klanner, DESY (1996) 142; R. Cashmore *et al.*, *ibid.*, 163.
- [4] M. Jonker *et al.* [CHARM Collaboration], *Phys. Lett. B* **86** (1979) 229.
- [5] C. Adloff *et al.* [H1 Collaboration], *Eur. Phys. J. C* **21** (2001) 33 [hep-ex/0012053].
- [6] C. Adloff *et al.* [H1 Collaboration], *Eur. Phys. J. C* **30** (2003) 1 [hep-ex/0304003].
- [7] H. Collaboration, *Eur. Phys. J. C* **63** (2009) 625 [arXiv:0904.0929 [hep-ex]].
- [8] F. D. Aaron *et al.* [H1 Collaboration], *Eur. Phys. J. C* **64** (2009) 561 [arXiv:0904.3513 [hep-ex]].
- [9] A. Arbuzov, D.Y. Bardin, J. Bluemlein, L. Kalinovskaya and T. Riemann, *Comput. Phys. Commun.* **94**, 128 (1996) [hep-ph/9511434].
- [10] A.A. Sokolov and I.M. Ternov, *Sov. Phys. Dokl.* **8** No. 12 (1964) 1203.
- [11] M. Beckmann *et al.*, *Nucl. Instrum. Meth. A* **479** (2002) 334.
- [12] D.P. Barber *et al.*, *Nucl. Instrum. Meth. A* **329** (1993) 79.
- [13] I. Abt *et al.* [H1 Collaboration], *Nucl. Instrum. Meth. A* **386** (1997) 310 and 348; R.D. Appuhn *et al.* [H1 SPACAL Group], *Nucl. Instrum. Meth. A* **386** (1997) 397.
- [14] G.A. Schuler and H. Spiesberger, Proceedings of the Workshop “Physics at HERA”, vol. 3, eds. W. Buchmüller, G. Ingelman, DESY (1992) 1419.
- [15] G. Ingelman, Proceedings of the Workshop “Physics at HERA”, vol. 3, eds. W. Buchmüller, G. Ingelman, DESY (1992) 1366.
- [16] A. Kwiatkowski, H. Spiesberger and H.-J. Möhring, *Comput. Phys. Commun.* **69** (1992) 155.
- [17] L. Lönnblad, *Comput. Phys. Commun.* **71** (1992) 15.
- [18] T. Sjöstrand and M. Bengtsson, *Comput. Phys. Commun.* **43** (1987) 367.
- [19] T. Sjöstrand, *Comput. Phys. Commun.* **82** (1994) 74.
- [20] H.L. Lai *et al.* [CTEQ Collaboration], *Eur. Phys. J. C* **12** (2000) 375 [hep-ph/9903282].
- [21] M. Glück, E. Reya and A. Vogt, *Phys. Rev. D* **46** (1992) 1973.
- [22] R. Brun *et al.*, GEANT3 User’s Guide, CERN-DD/EE-84-1 (1987).

- [23] B. Porthault, Ph.D. thesis (March 2005), LAL 05-05 (IN2P3/CNRS), Université de Paris-Sud XI, Orsay, available at http://www-h1.desy.de/publications/theses_list.html.
- [24] A. Blondel and F. Jacquet, Proceedings of the Study of an *ep* Facility for Europe, ed. U. Amaldi, DESY (1979) 391.
- [25] A. Aktas, Ph.D. thesis (August 2005), Hamburg University, available at http://www-h1.desy.de/publications/theses_list.html.
- [26] R. Plačákytė, Ph.D. thesis (June 2006) , Max-Planck-Institut für Physik, Munich, will be available at http://www-h1.desy.de/publications/theses_list.html.
- [27] B. Antunovic, Ph.D. thesis (September 2007), Max-Planck-Institut für Physik, Munich, will be available at http://www-h1.desy.de/publications/theses_list.html.
- [28] W. Lorenzon [HERMES Collaboration], DESY-HERMES-97-68, *7th International Workshop on Polarized Gas Targets and Polarized Beams*, Urbana, IL, 18-22 Aug 1997; F. Corriveau *et al.* [TPOL Polarimeter Group], “A Calibration of the HERA Transverse Polarimeter for the 2003/2004 Data”, available at <http://www.desy.de/~pol2000/documents/documents.html>.
- [29] C. Adloff *et al.* [H1 Collaboration], Eur. Phys. J. C **19** (2001) 269 [hep-ex/0012052].
- [30] G.J. Feldman and R.D. Cousins, Phys. Rev. D **57** (1998) 3873 [physics/9711021].
- [31] C. Adloff *et al.* [H1 Collaboration], Eur. Phys. J. C **13**, 609 (2000) [arXiv:hep-ex/9908059].

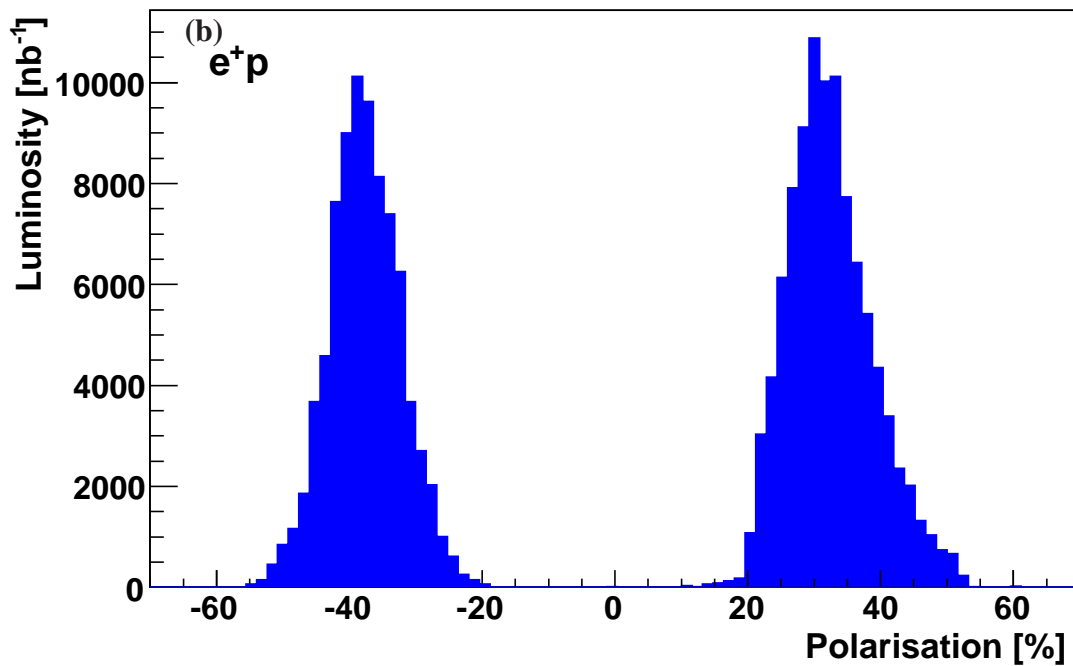
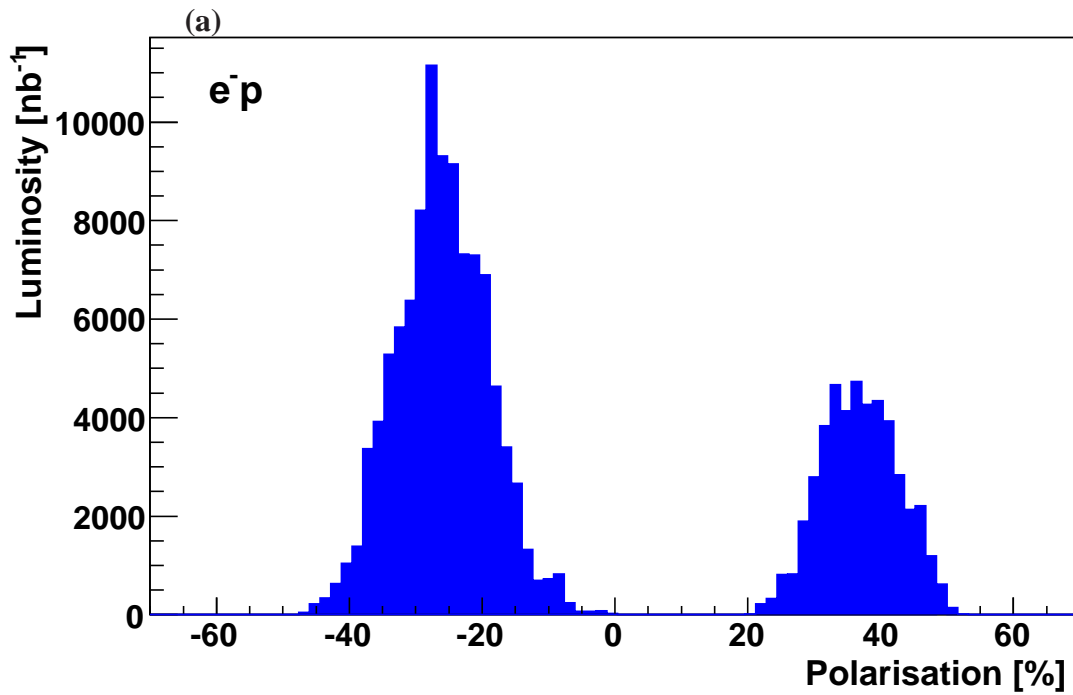


Figure 1: The polarisation profile weighted by the luminosity values for the (a) e^-p data and (b) e^+p data. The $L(R)$ sample corresponds to distribution having negative (positive) polarisation values.

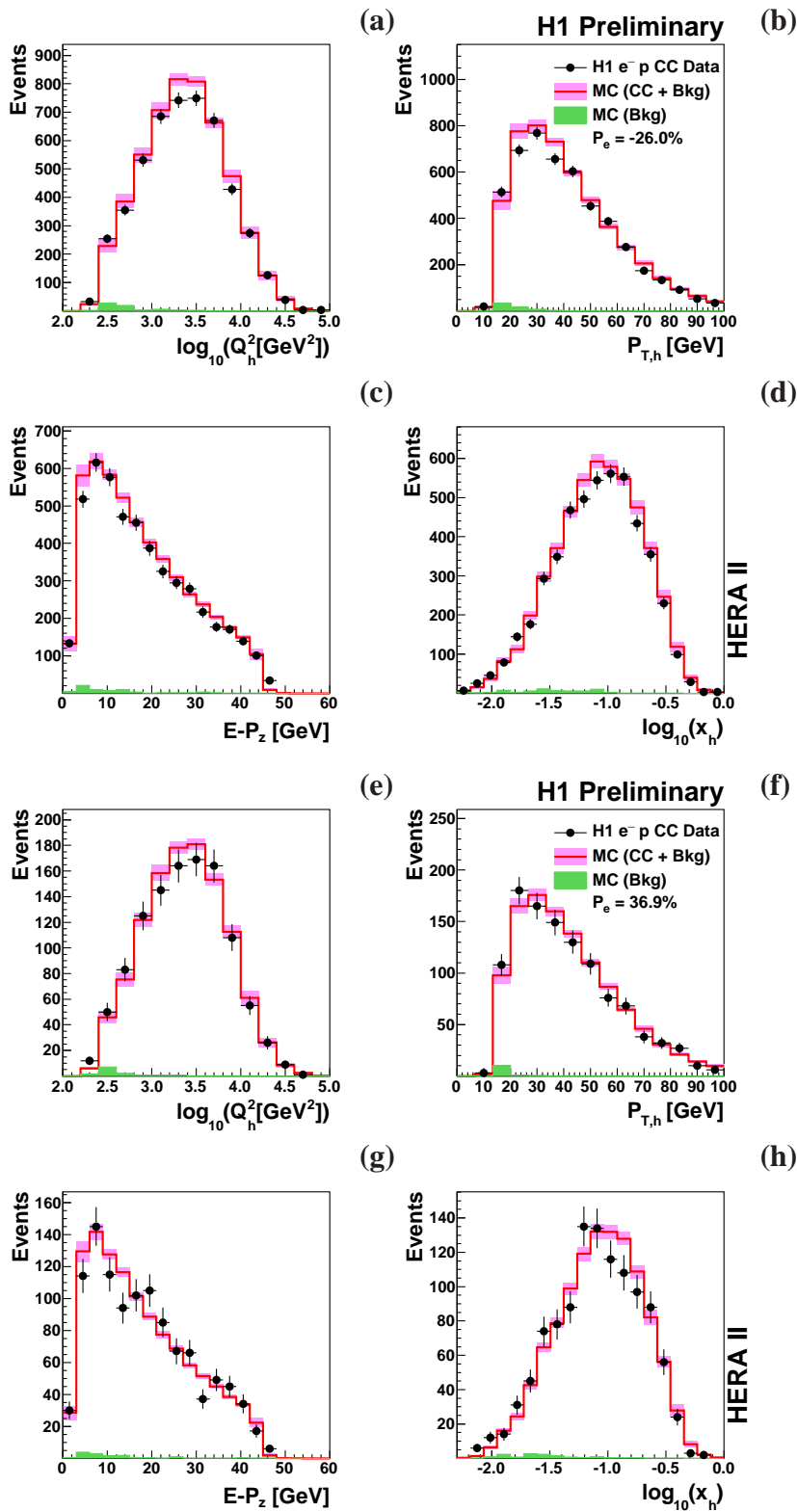


Figure 2: Distributions of (a,e) $\log_{10} Q_h^2$, (b,f) $P_{T,h}$, (c,g) $E - P_Z$ and (d,h) $\log_{10} x_h$ shown in upper and lower plots for the selected events in the (a-d) $e^-p L$ and (e-h) $e^-p R$ data sets. The Monte Carlo (MC) contributions from the charged current (CC) process and the ep background (bkg) processes are shown as the full line, the total uncertainty is represented by the shaded band. The contribution from the ep background is shown as the lower shaded histogram.

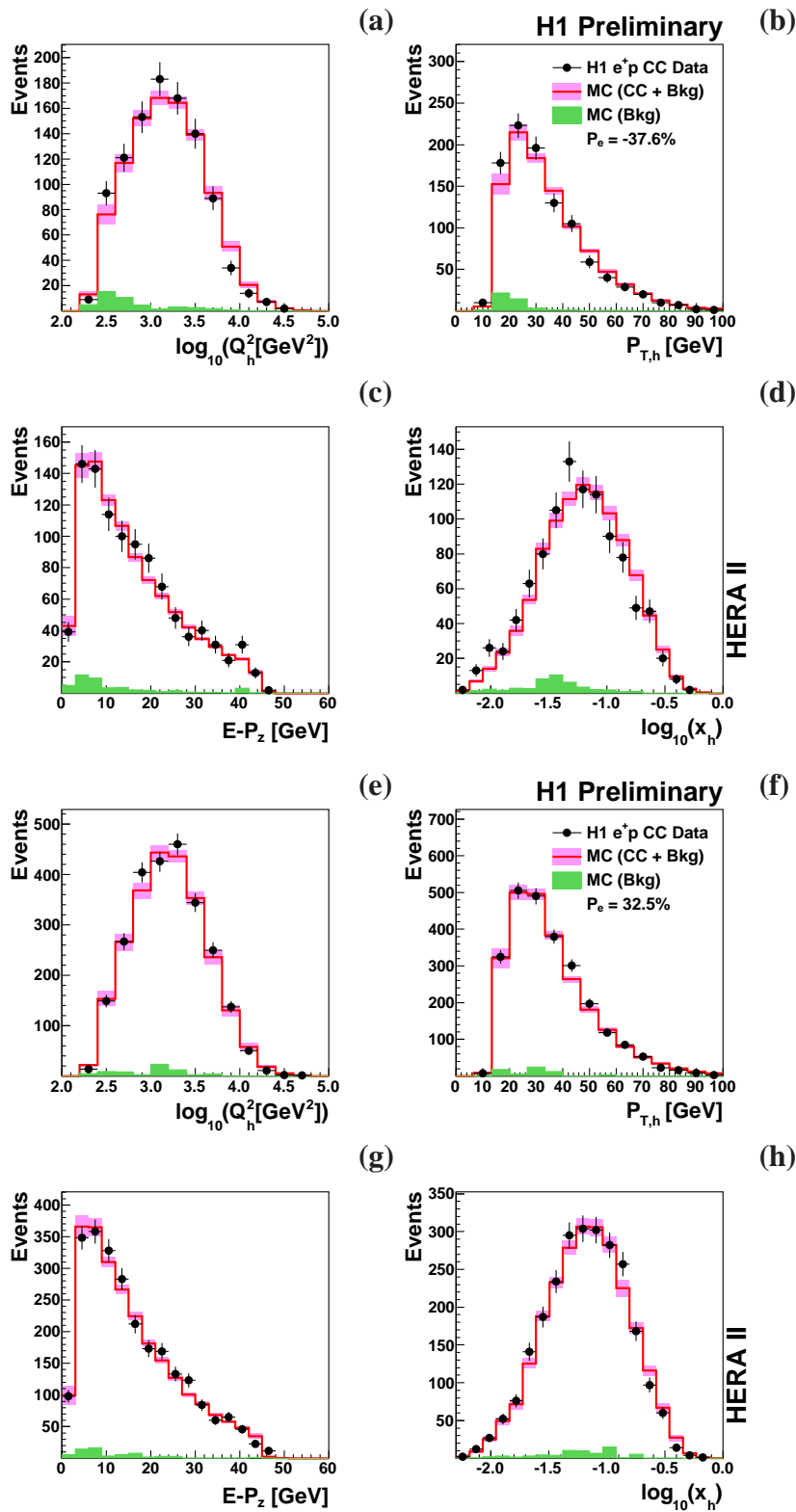


Figure 3: Distributions of (a,e) $\log_{10} Q_h^2$, (b,f) $P_{T,h}$, (c,g) $E - P_Z$ and (d,h) $\log_{10} x_h$ shown in upper and lower plots for the selected events in the (a-d) $e^-p L$ and (e-h) $e^+p R$ data sets. The Monte Carlo (MC) contributions from the charged current (CC) process and the ep background (bkg) processes are shown as the full line, the total uncertainty is represented by the shaded band. The contribution from the ep background is shown as the lower shaded histogram.

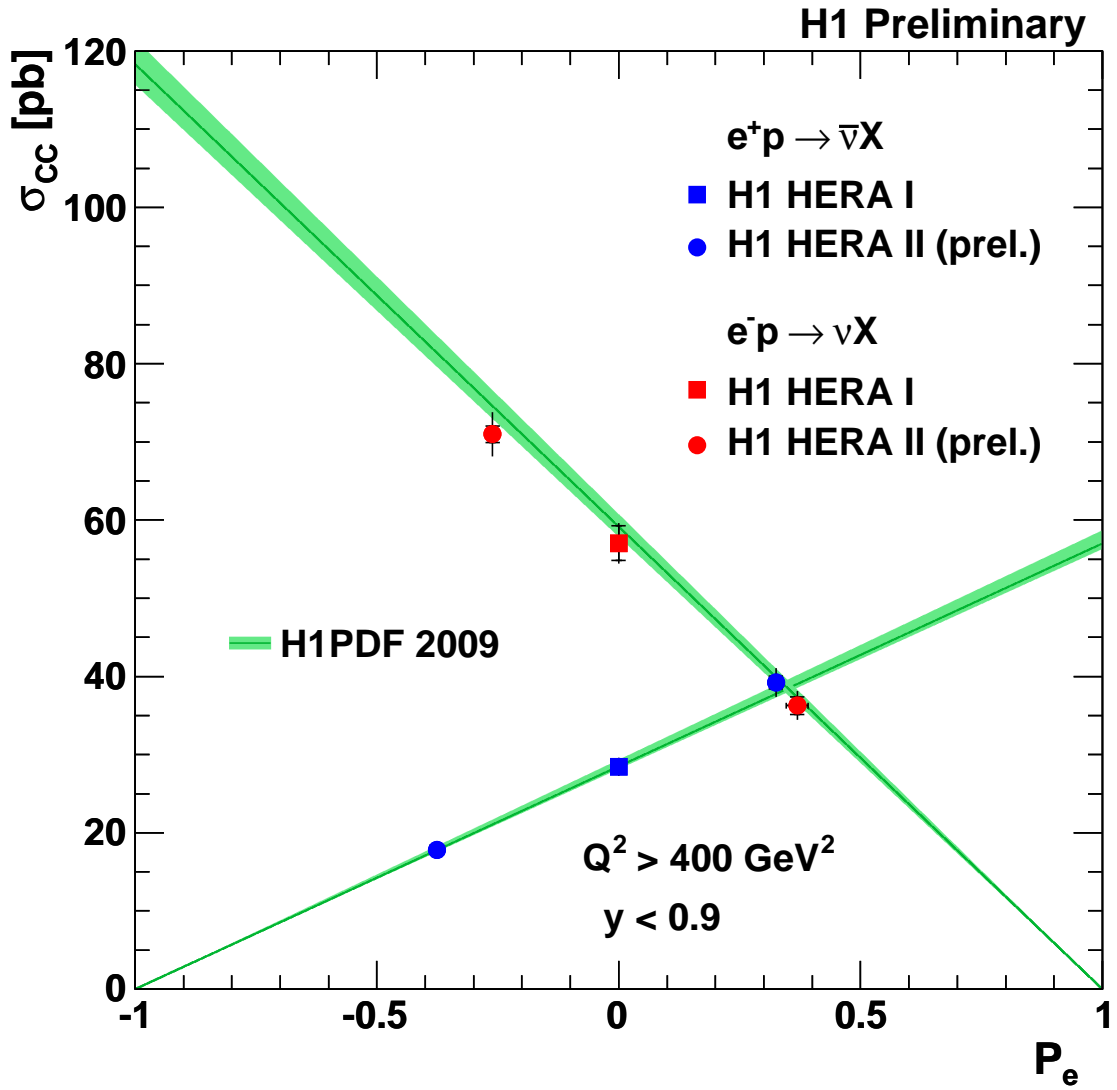


Figure 4: The dependence of the $e^\pm p$ CC cross section on the lepton beam polarisation P_e . The inner and outer error bars represent respectively the statistical and total errors. The uncertainties on the polarisation measurement are smaller than the symbol size. The data are compared to the Standard Model prediction based on the H1 PDF 2009 parametrisation (dark shaded band). The light shaded band corresponds to the resulting one-sigma contour of a linear fit to the data shown as the central line.

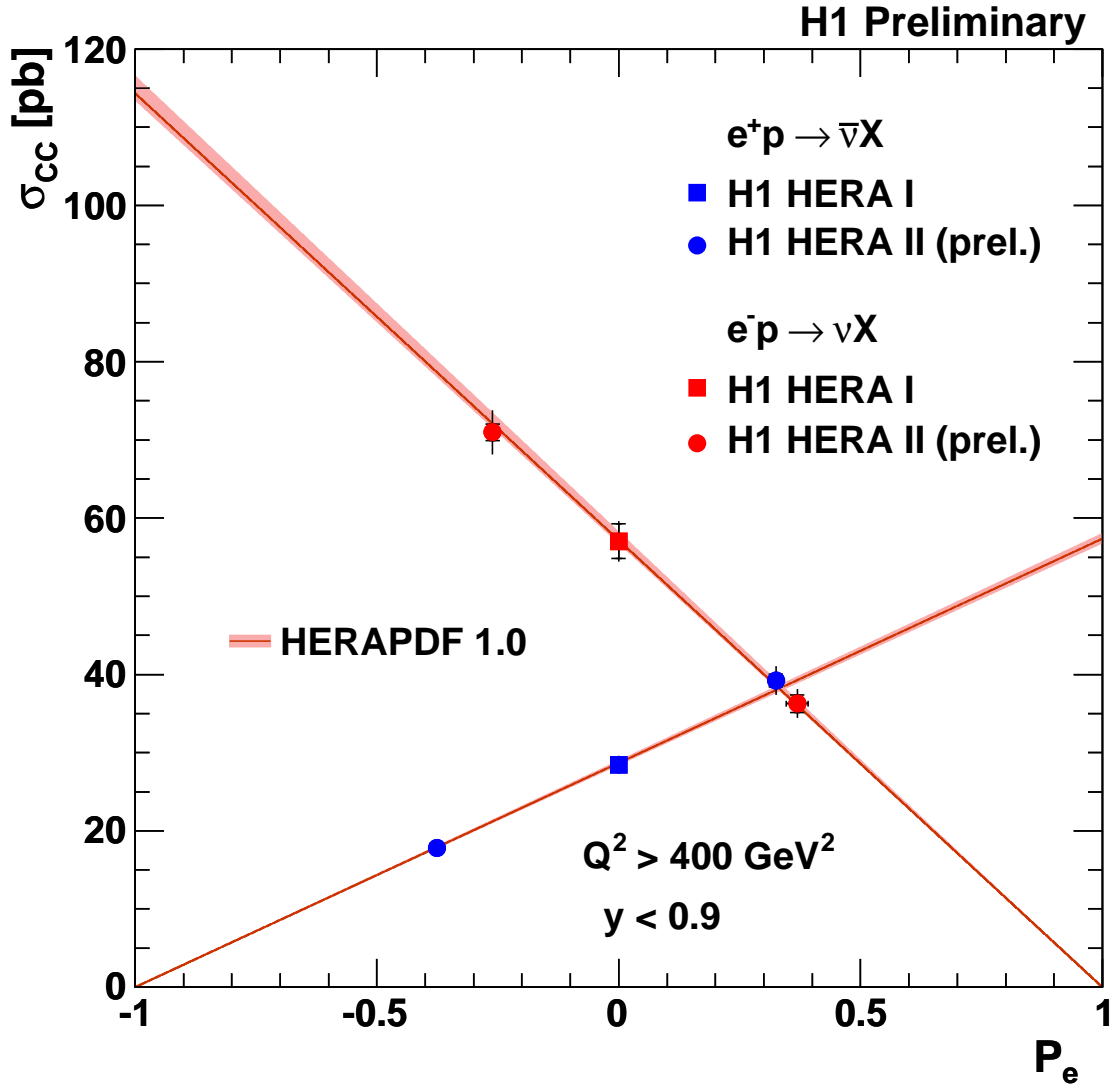


Figure 5: The dependence of the $e^\pm p$ CC cross section on the lepton beam polarisation P_e . The inner and outer error bars represent respectively the statistical and total errors. The uncertainties on the polarisation measurement are smaller than the symbol size. The data are compared to the Standard Model prediction based on the HERAPDF 1.0 parametrisation (dark shaded band). The light shaded band corresponds to the resulting one-sigma contour of a linear fit to the data shown as the central line.

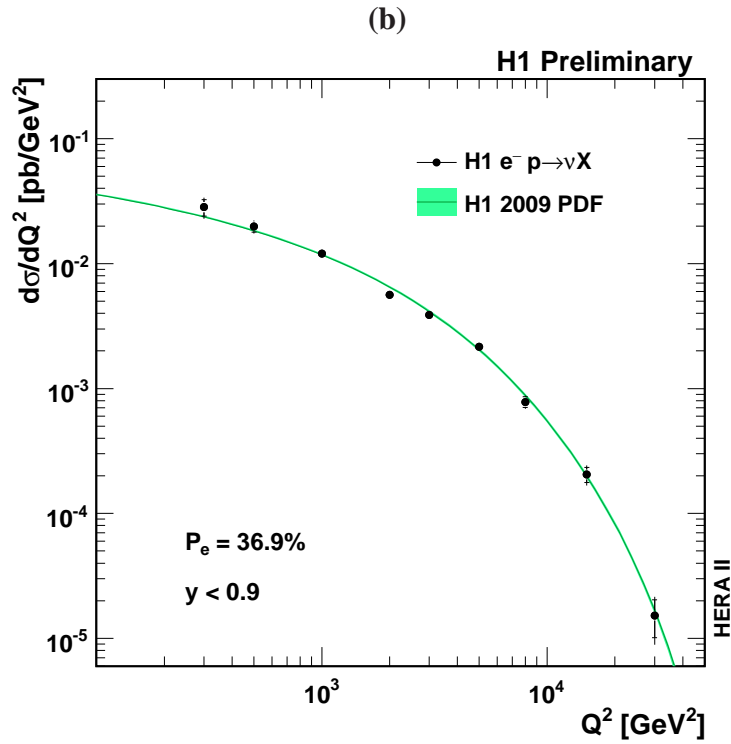
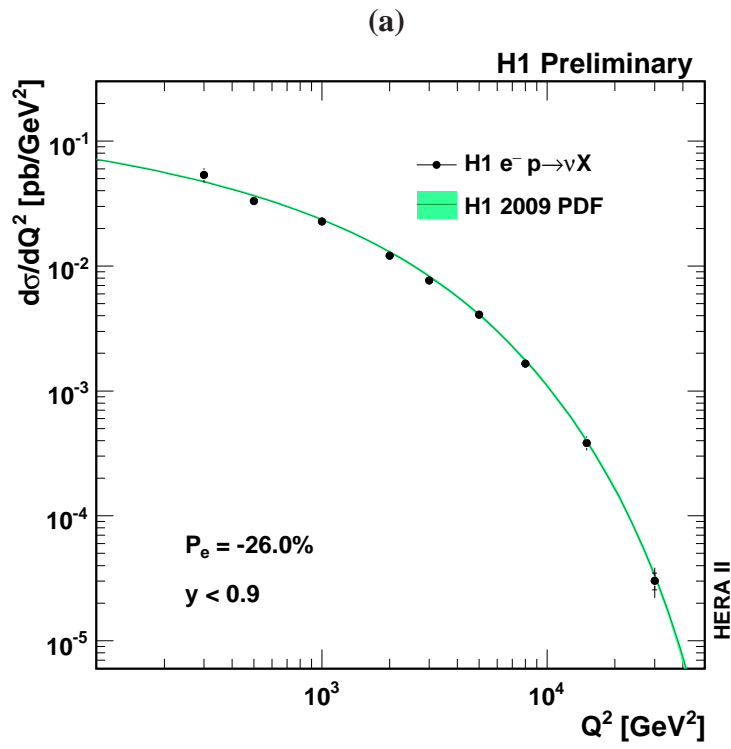


Figure 6: The Q^2 dependences of the CC cross section $d\sigma/dQ^2$, shown for the e^-p data (solid points) using the L (a) and R (b) polarised samples. The results are compared with the corresponding Standard Model expectations determined from the H1 PDF 2000 fit. The inner and outer error bars represent respectively the statistical and total errors.

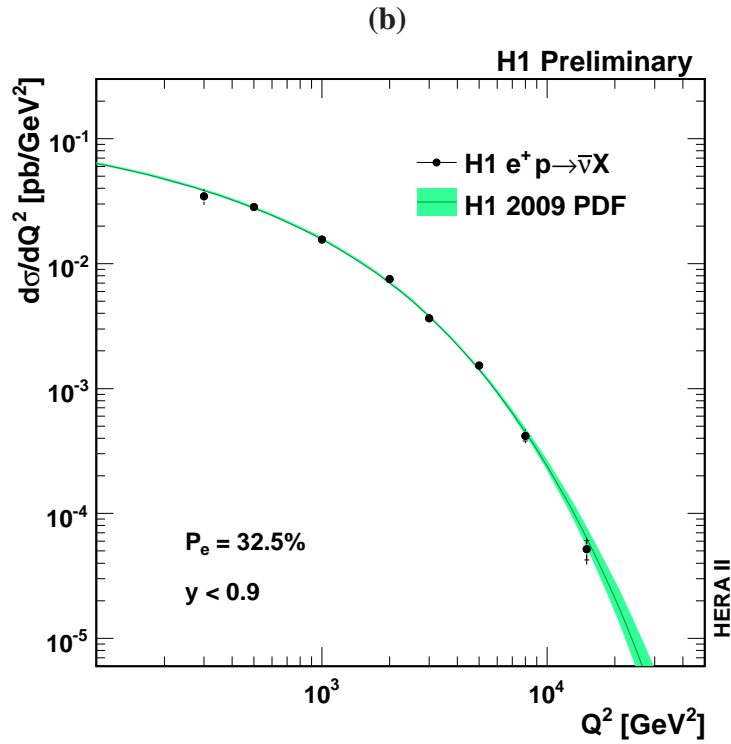
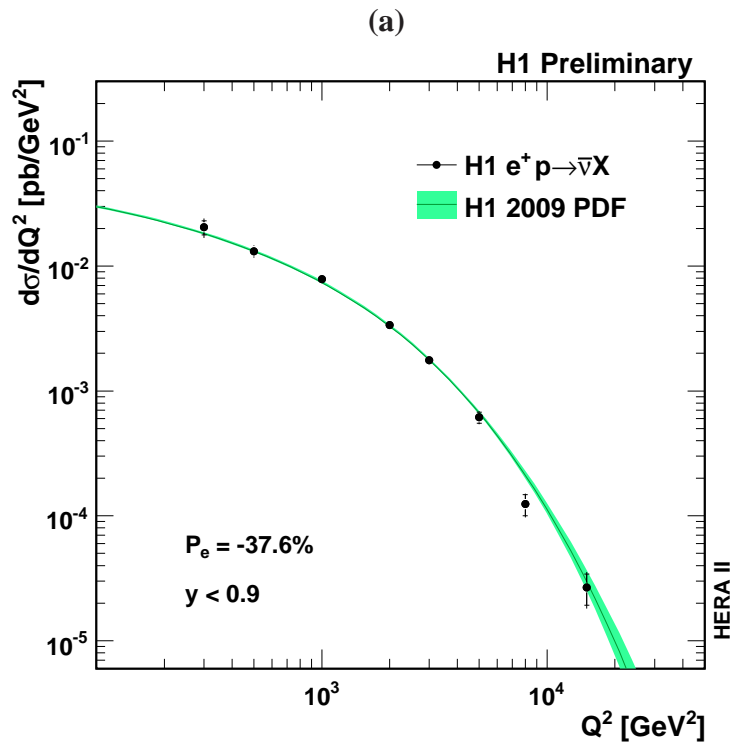


Figure 7: The Q^2 dependences of the CC cross section $d\sigma/dQ^2$, shown for the e^+p data (solid points) using the L (a) and R (b) polarised samples. The results are compared with the corresponding Standard Model expectations determined from the H1 PDF 2000 fit. The inner and outer error bars represent respectively the statistical and total errors.

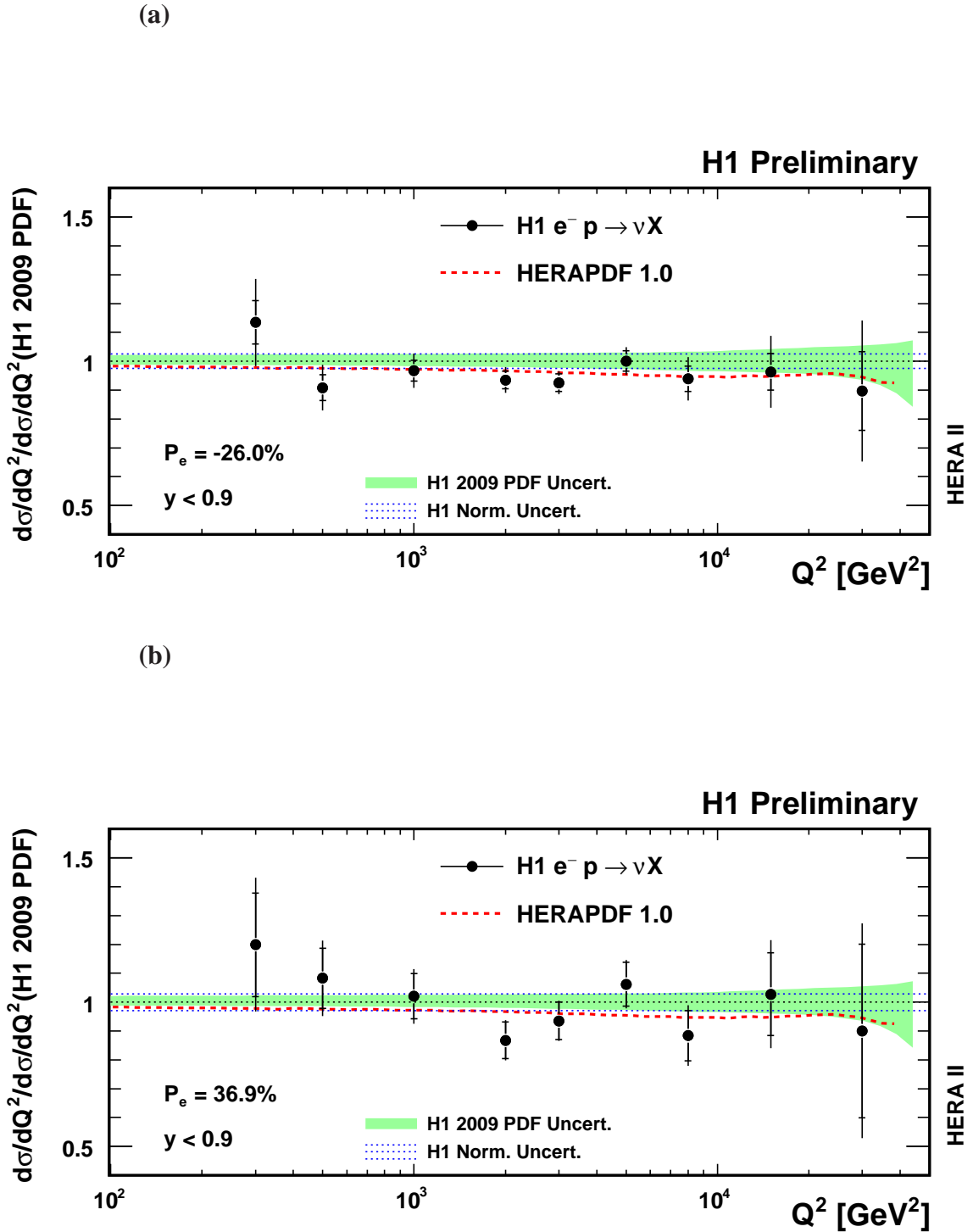


Figure 8: The Q^2 dependences of the CC cross section ratio $d\sigma/dQ^2$ for e^-p scattering using the L (a) and R (b) polarised data samples, to the Standard Model expectation obtained from H1 PDF 2009 (green band). In addition the ratio using the expectation from HERAPDF1.0 is also shown (dashed line). The inner error bars represent the statistical uncertainties and the outer error bars represent the total errors. The normalisation uncertainty is not included in the error bars and is instead represented by the blue dashed lines.

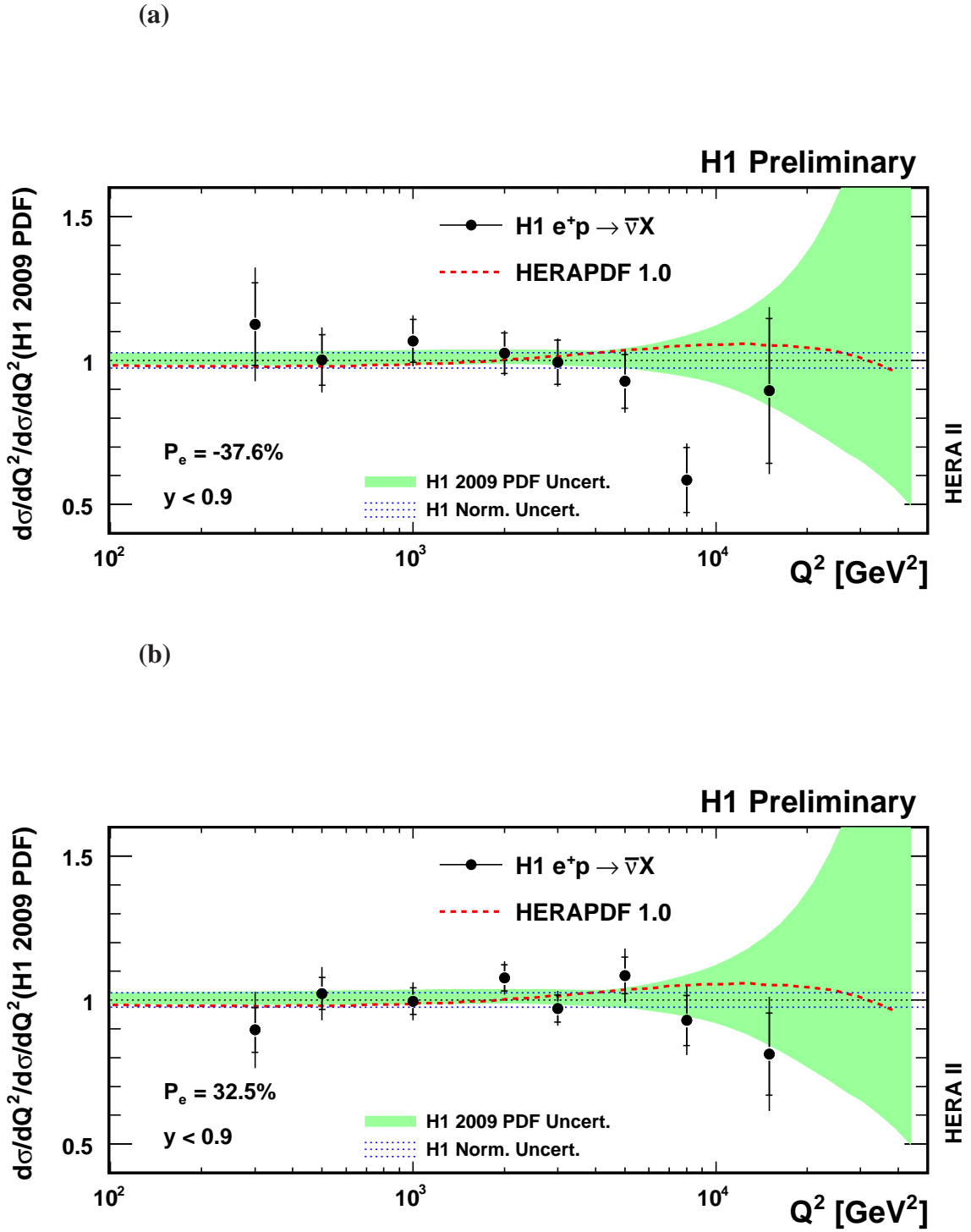


Figure 9: The Q^2 dependences of the CC cross section ratio $d\sigma/dQ^2$ for e^+p scattering using the L (a) and R (b) polarised data samples, to the Standard Model expectation obtained from H1 PDF 2009 (green band). In addition the ratio using the expectation from HERAPDF1.0 is also shown (dashed line). The inner error bars represent the statistical uncertainties and the outer error bars represent the total errors. The normalisation uncertainty is not included in the error bars and is instead represented by the blue dashed lines.

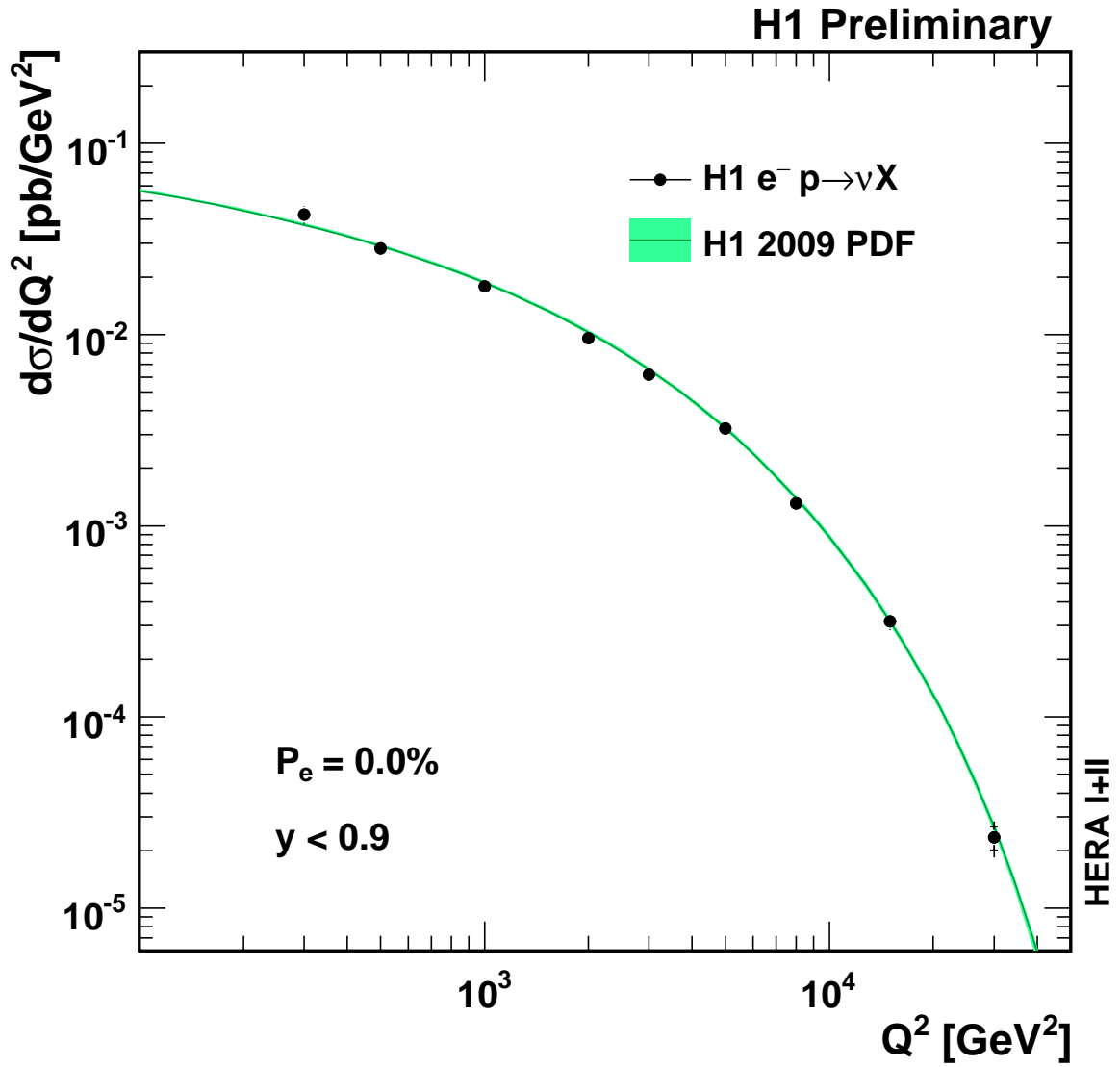


Figure 10: The Q^2 dependence of the unpolarised CC cross section $d\sigma/dQ^2$, shown for the $e^- p$ data (solid points) using the complete HERA-I+II data set. The results are compared with the corresponding Standard Model expectations determined from the H1 PDF 2000 fit. The inner and outer error bars represent respectively the statistical and total errors.

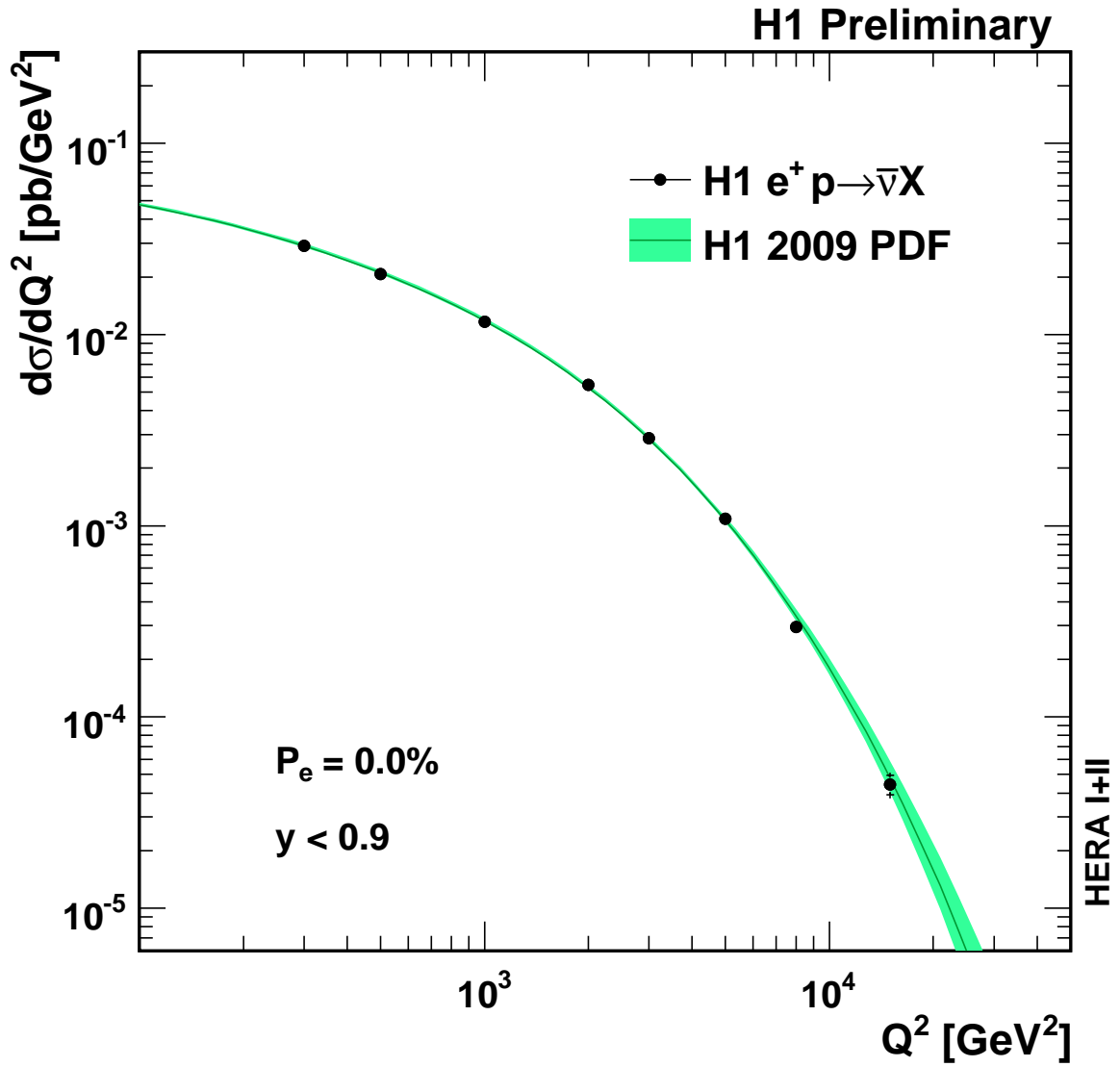


Figure 11: The Q^2 dependence of the unpolarised CC cross section $d\sigma/dQ^2$, shown for the e^+p data (solid points) using the complete HERA-I+II data set. The results are compared with the corresponding Standard Model expectations determined from the H1 PDF 2000 fit. The inner and outer error bars represent respectively the statistical and total errors.

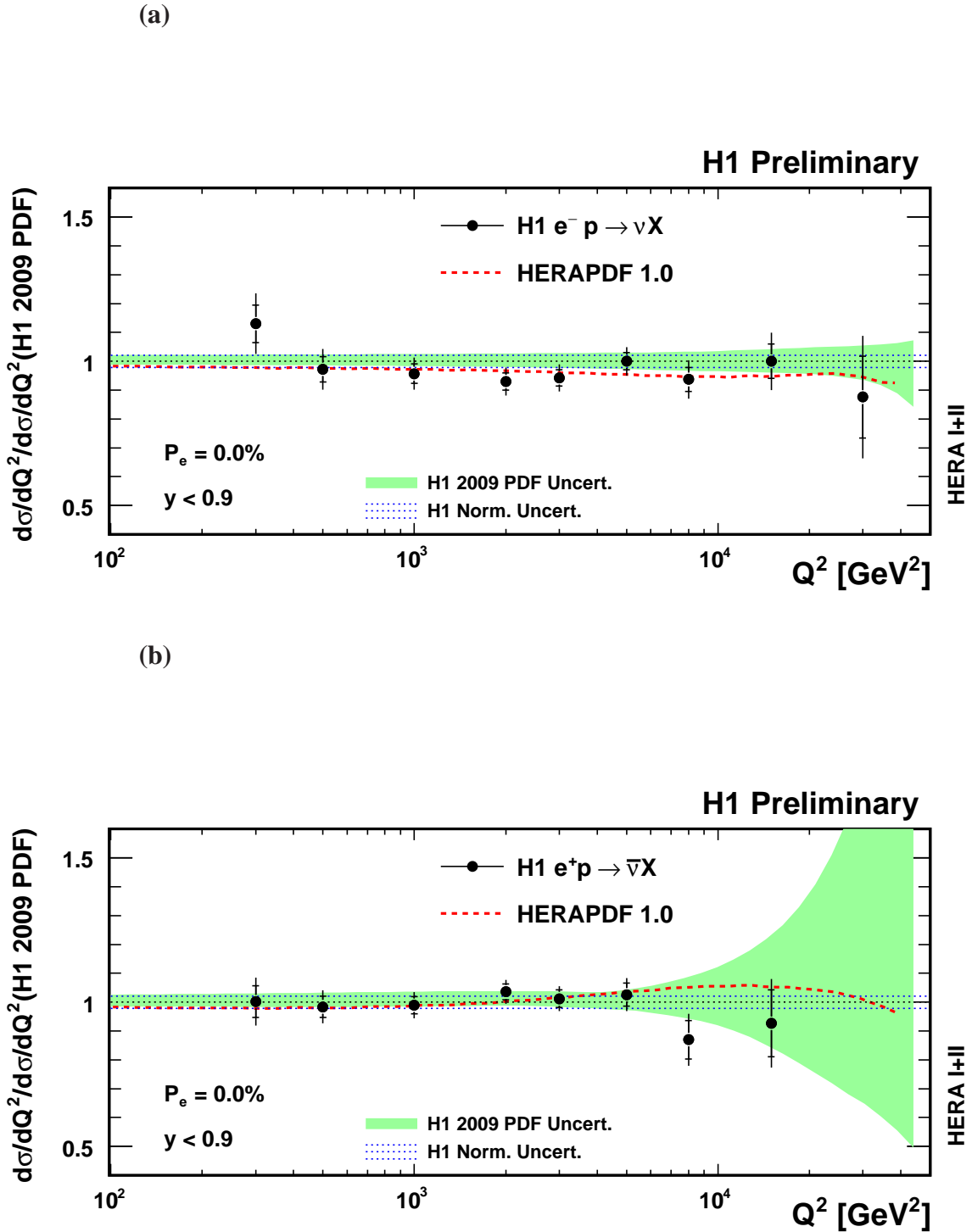


Figure 12: The Q^2 dependences of the CC cross section ratio $d\sigma/dQ^2$ for e^-p scattering (a) and e^+p scattering (b) polarised data samples, to the Standard Model expectation obtained from H1 PDF 2009 (green band). The measurements use the complete HERA-I+II data set. In addition the ratio using the expectation from HERAPDF1.0 is also shown (dashed line). The inner error bars represent the statistical uncertainties and the outer error bars represent the total errors. The normalisation uncertainty is not included in the error bars and is instead represented by the blue dashed lines.

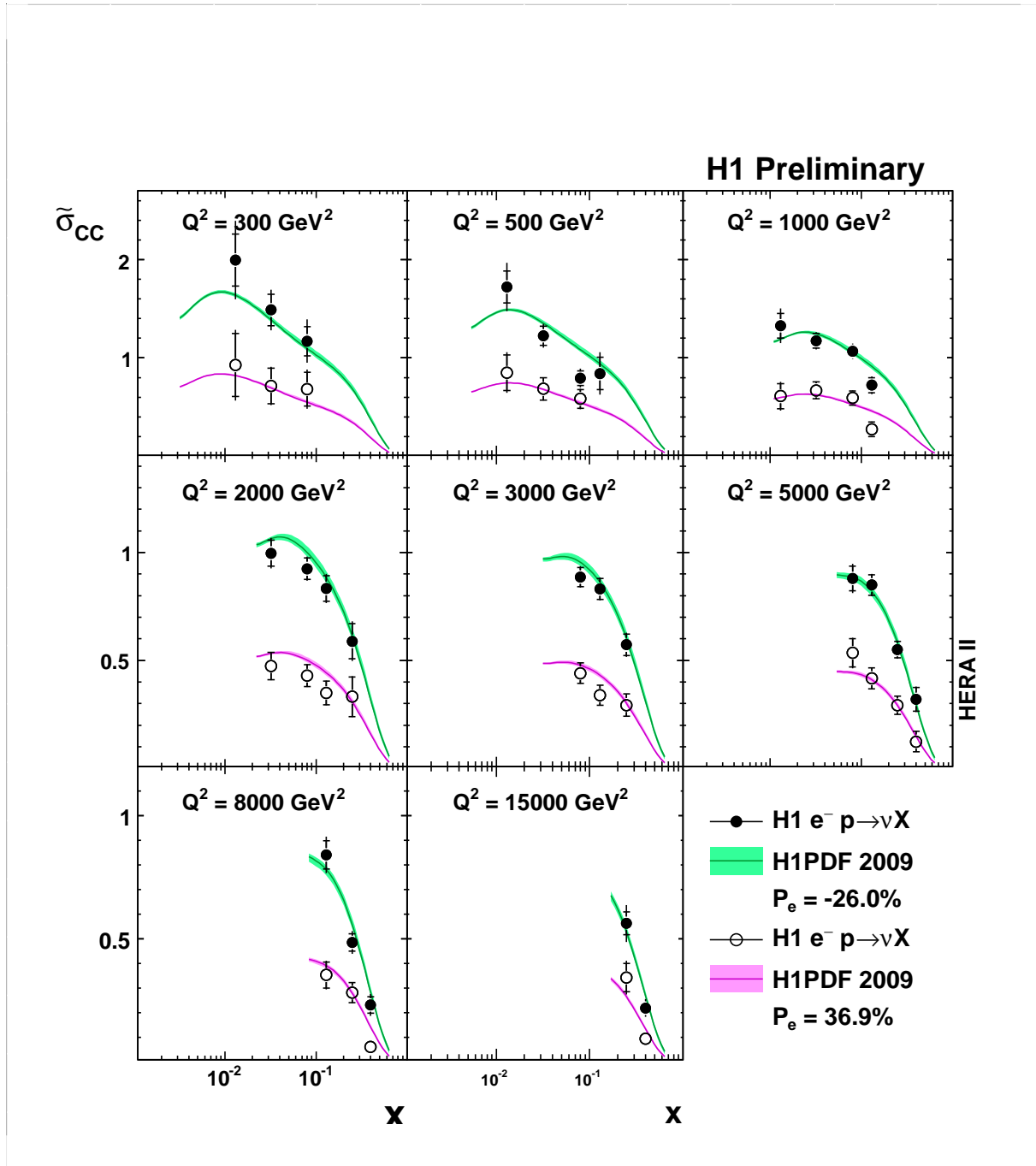


Figure 13: The reduced cross section $\tilde{\sigma}_{CC}$ in polarised e^-p scattering using the L (solid points) and R (open points) data sets. The data are compared to the Standard Model prediction from H1 PDF 2009. The inner error bars represent the statistical uncertainties and the outer error bars represent the total errors. The normalisation uncertainty is not included in the error bars.

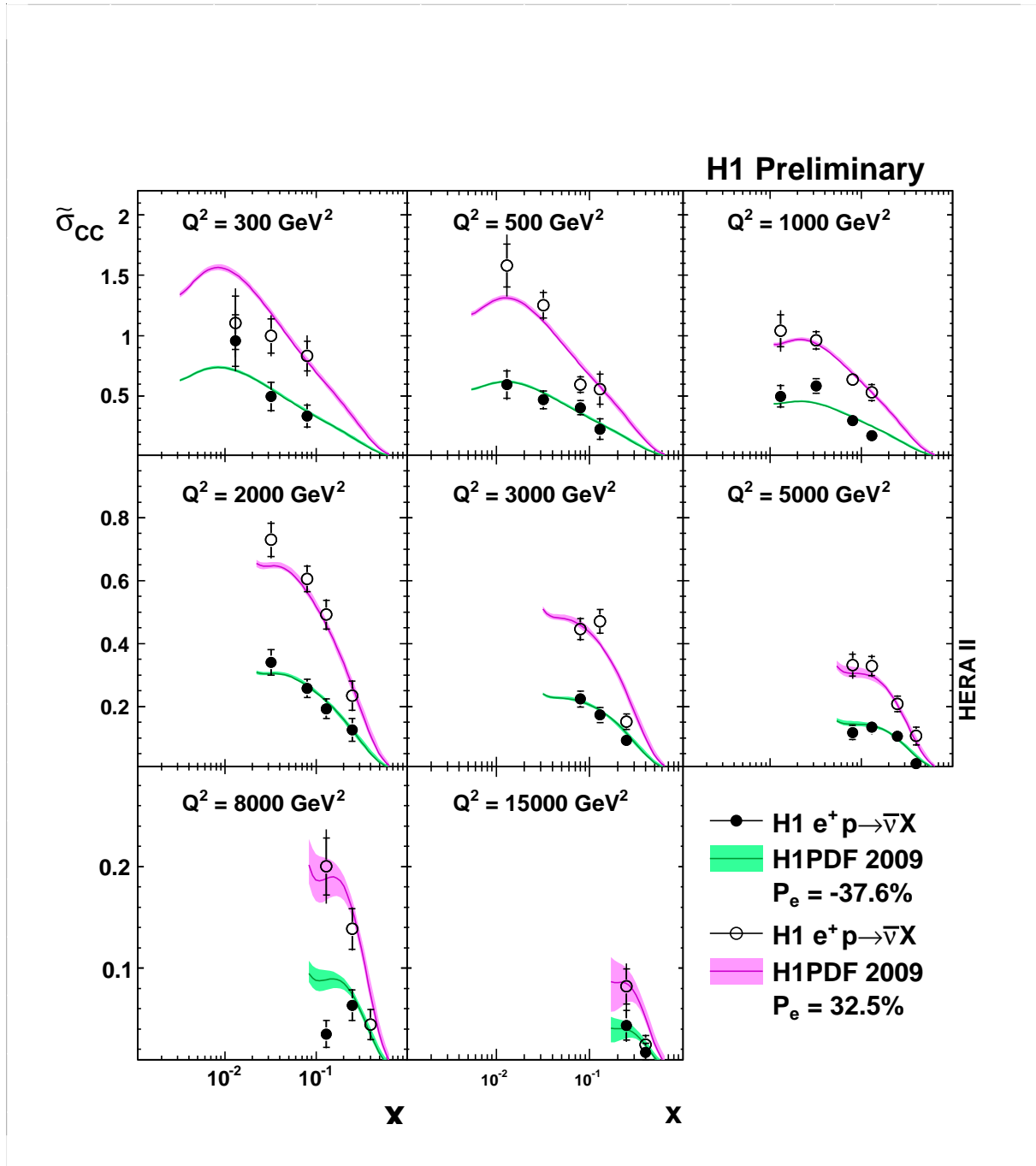


Figure 14: The reduced cross section $\tilde{\sigma}_{CC}$ in polarised e^+p scattering using the L (solid points) and R (open points) data sets. The data are compared to the Standard Model prediction from H1 PDF 2009. The inner error bars represent the statistical uncertainties and the outer error bars represent the total errors. The normalisation uncertainty is not included in the error bars.

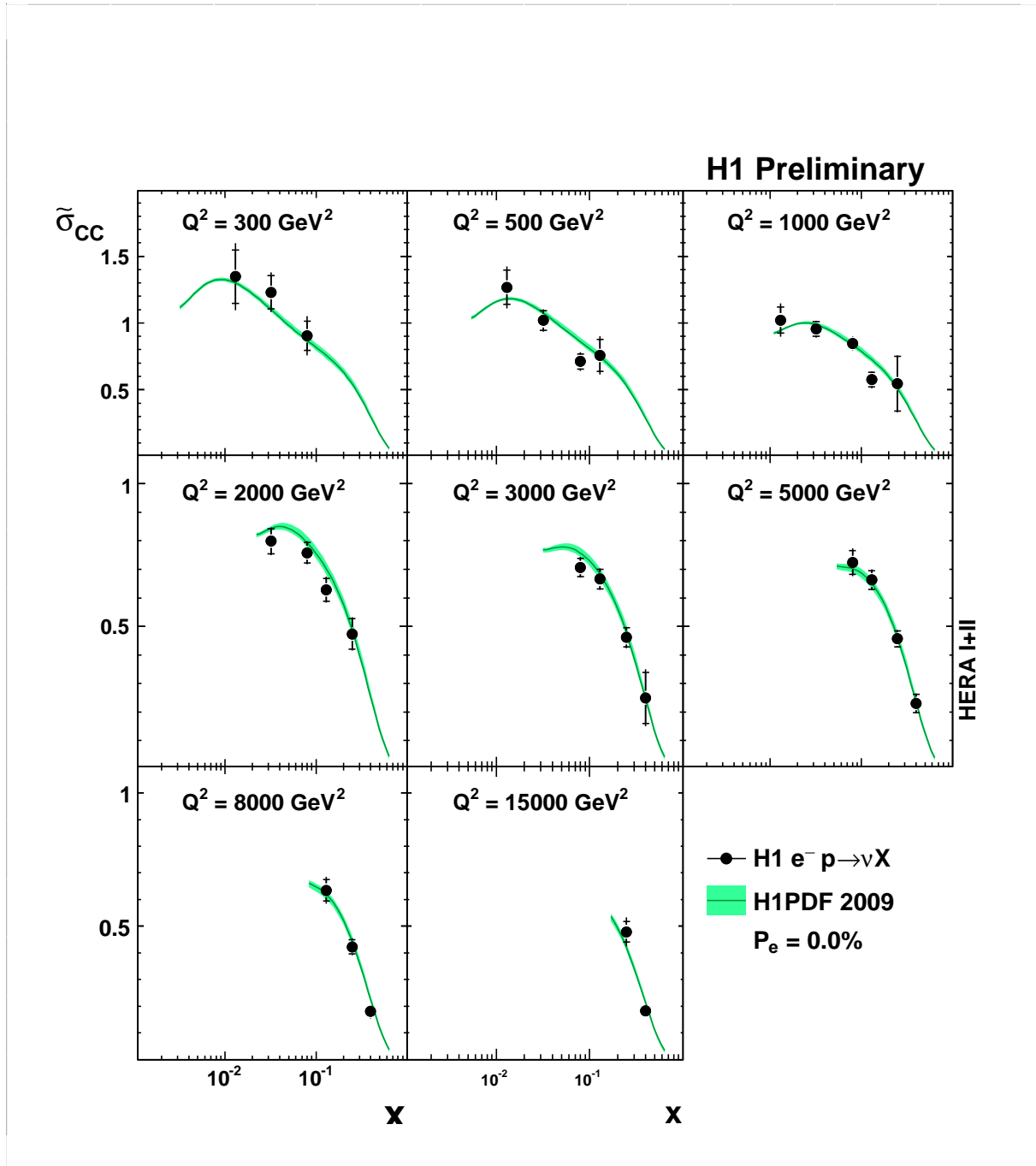


Figure 15: The reduced cross section $\tilde{\sigma}_{CC}$ in unpolarised $e^- p$ scattering using the complete HERA-I+II data sets. The data are compared to the Standard Model prediction from H1 PDF 2009. The inner error bars represent the statistical uncertainties and the outer error bars represent the total errors. The normalisation uncertainty is not included in the error bars.

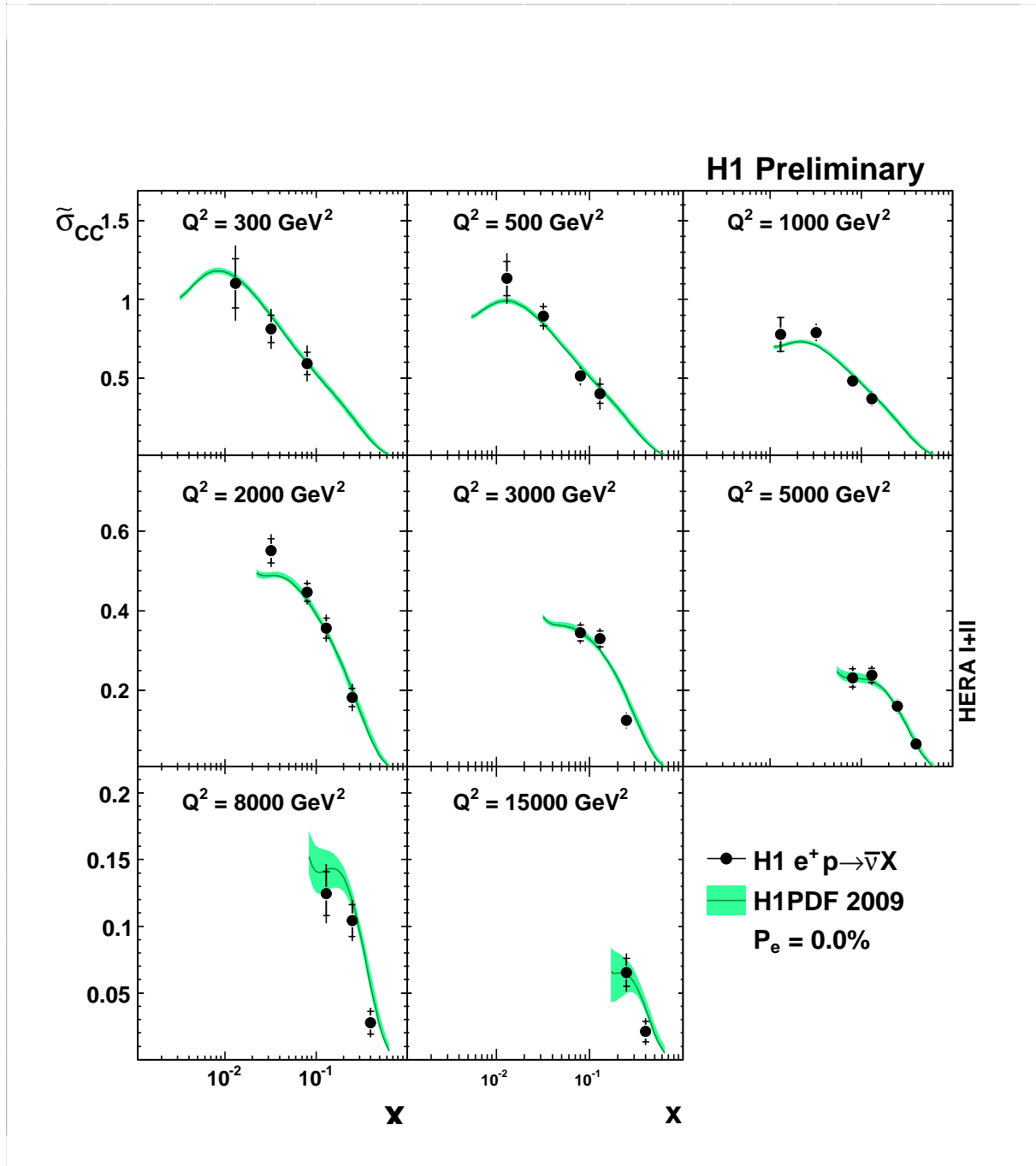


Figure 16: The reduced cross section $\tilde{\sigma}_{CC}$ in unpolarised e^+p scattering using the complete HERA-I+II data sets. The data are compared to the Standard Model prediction from H1 PDF 2009. The inner error bars represent the statistical uncertainties and the outer error bars represent the total errors. The normalisation uncertainty is not included in the error bars.

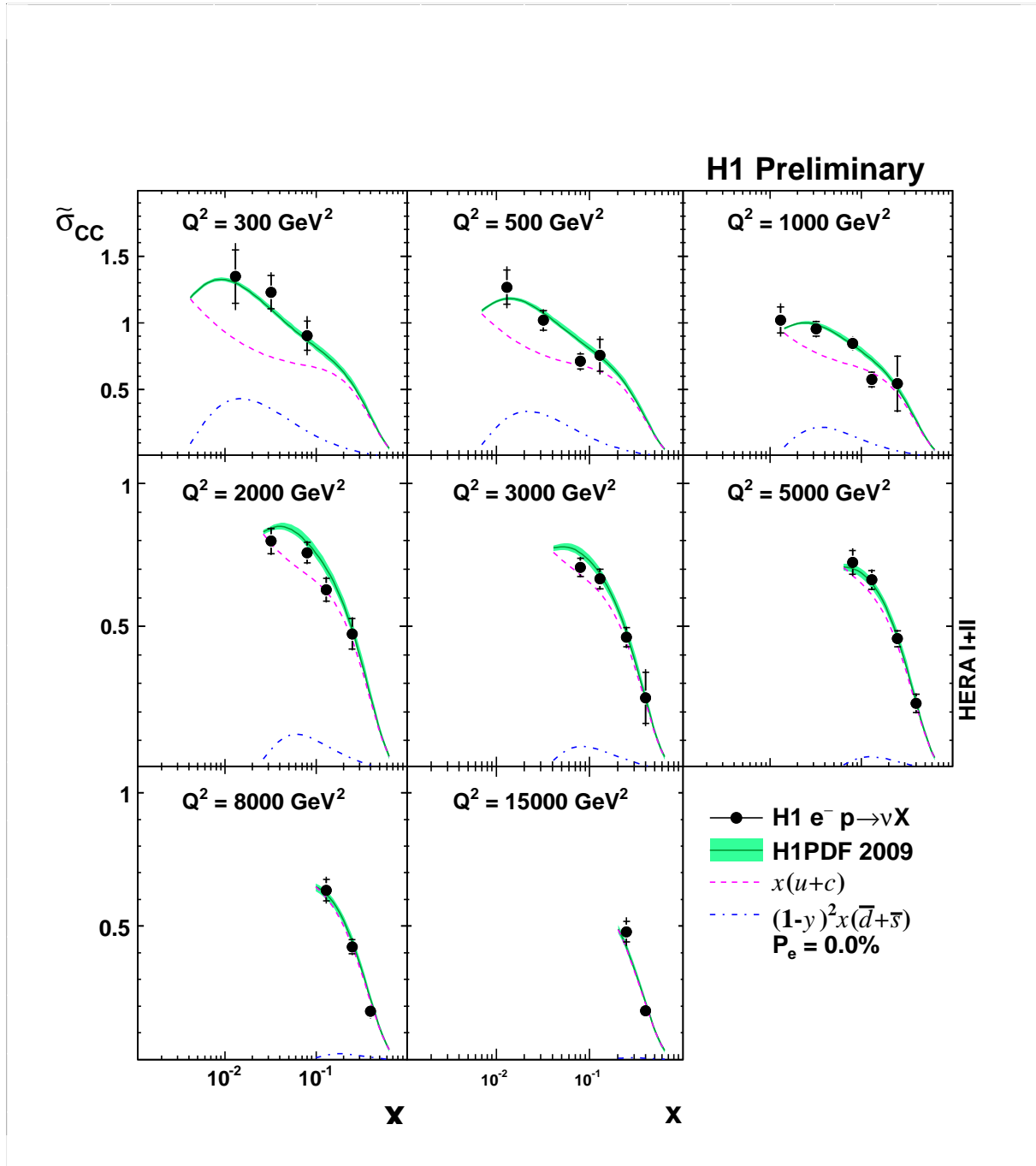


Figure 17: The reduced cross section $\tilde{\sigma}_{CC}$ in unpolarised e^-p scattering using the complete HERA-I+II data sets. The data are compared to the Standard Model prediction from H1 PDF 2009. The inner error bars represent the statistical uncertainties and the outer error bars represent the total errors. The normalisation uncertainty is not included in the error bars. The separate contributions from quarks and anti-quarks are shown as the dashed and dashed-dotted curves.

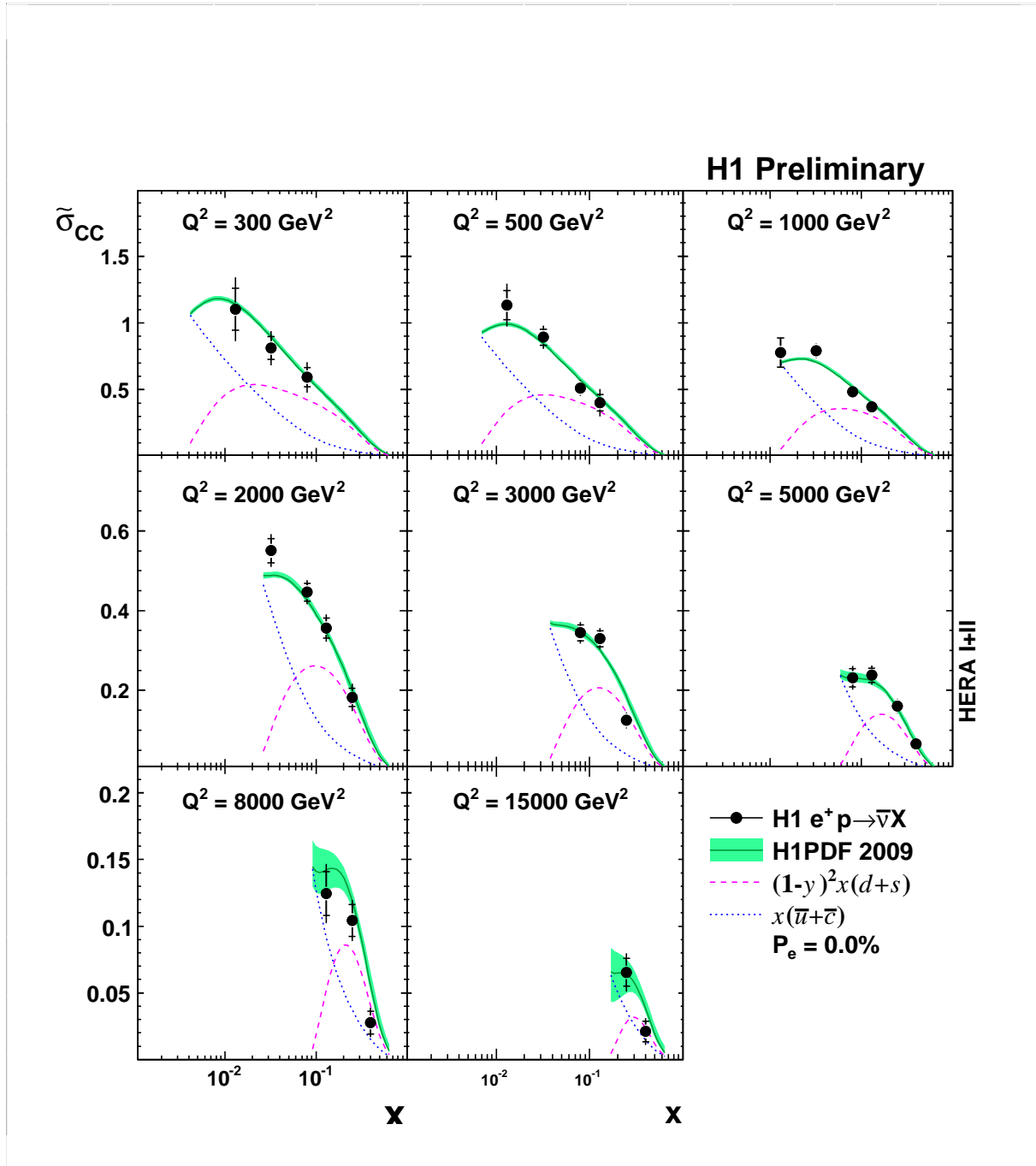


Figure 18: The reduced cross section $\tilde{\sigma}_{CC}$ in unpolarised e^+p scattering using the complete HERA-I+II data sets. The data are compared to the Standard Model prediction from H1 PDF 2009. The inner error bars represent the statistical uncertainties and the outer error bars represent the total errors. The normalisation uncertainty is not included in the error bars. The separate contributions from quarks and anti-quarks are shown as the dashed and dashed-dotted curves.

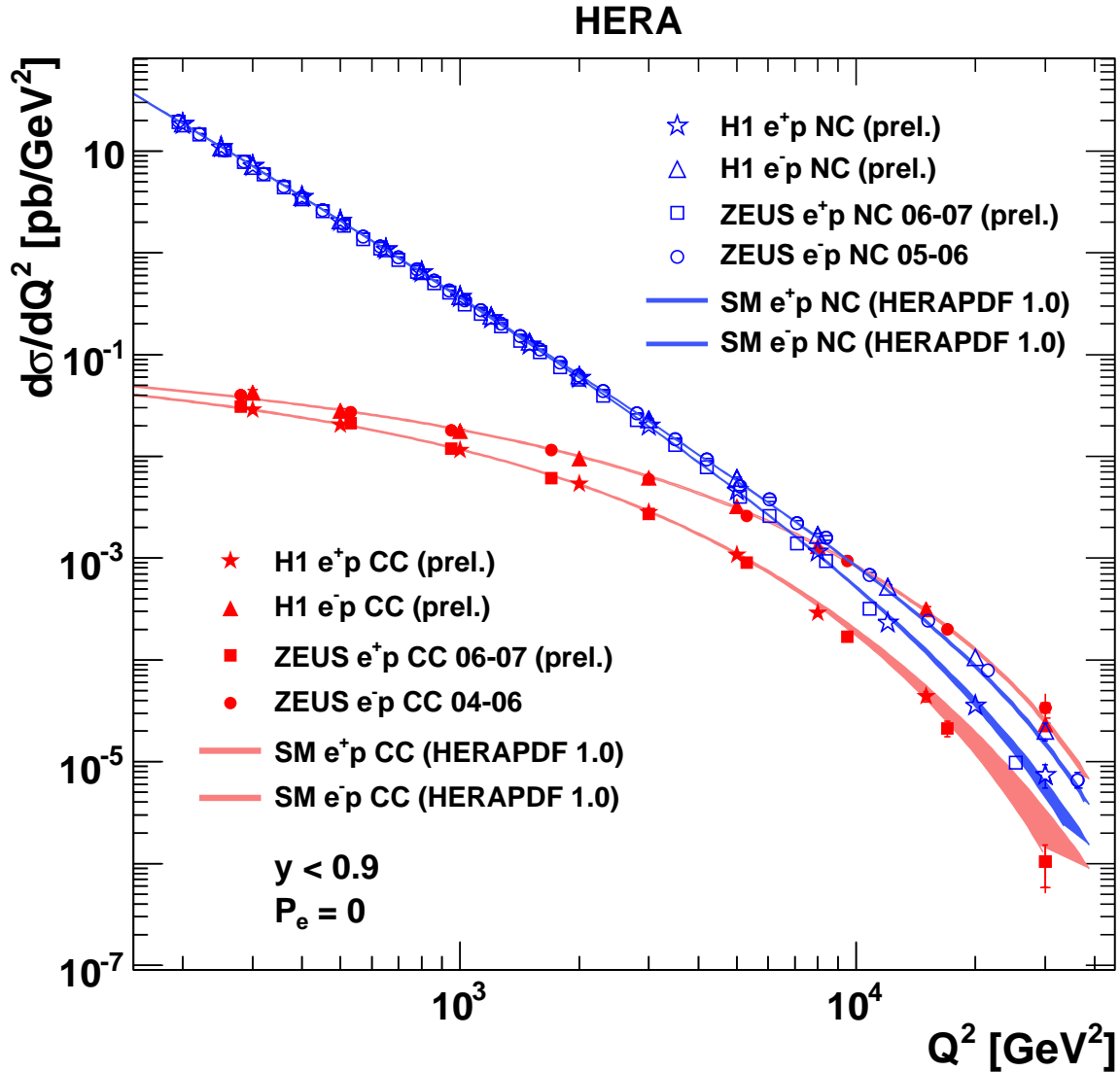


Figure 19: The Q^2 dependence of the unpolarised NC and CC cross sections $d\sigma/dQ^2$, shown for the e^+p (open points) and e^-p (solid points) scattering data from the H1 and ZEUS collaborations. The results are compared with the corresponding Standard Model expectations determined from the HERAPDF 1.0 fit. The inner and outer error bars represent respectively the statistical and total errors.